

# Optimal control of vortex core polarity by resonant microwave pulses

Benjamin Pigeau,<sup>1</sup> Grégoire de Loubens,<sup>1,\*</sup> Olivier Klein,<sup>1</sup> Andreas Riegler,<sup>2</sup> Florian Lochner,<sup>2</sup> Georg Schmidt,<sup>2,†</sup> and Laurens W. Molenkamp<sup>2</sup>

<sup>1</sup>*Service de Physique de l'État Condensé (CNRS URA 2464),  
CEA Saclay, 91191 Gif-sur-Yvette, France*

<sup>2</sup>*Physikalisches Institut (EP3), Universität Würzburg, 97074 Würzburg, Germany*

(Dated: July 29, 2011)

## Abstract

In a vortex-state magnetic nano-disk<sup>1–3</sup>, the static magnetization is curling in the plane, except in the core region where it is pointing out-of-plane<sup>4,5</sup>, either up or down leading to two possible stable states of opposite core polarity  $p$ . Dynamical reversal of  $p$  by large amplitude motion of the vortex core has recently been demonstrated experimentally<sup>6–10</sup>, raising fundamental interest<sup>11–14</sup> for potential application in magnetic storage devices<sup>15</sup>. Here we demonstrate coherent control of  $p$  by single and double microwave pulse sequences, taking advantage of the resonant vortex dynamics in a perpendicular bias magnetic field<sup>16</sup>. Optimization of the microwave pulse duration required to switch  $p$  allows to experimentally infer the characteristic decay time of the vortex core in the large oscillation regime. It is found to be more than twice shorter than in the small oscillation regime, raising the fundamental question of the non-linear behaviour of magnetic dissipation.

Magnetic vortices are topological solitons with rich dynamical properties. The lowest energy excitation of the vortex ground state is the so-called gyrotropic mode<sup>3</sup>, corresponding to the gyration of the vortex core around its equilibrium position with a frequency in the sub-gigahertz range<sup>17,18</sup>. It is now established experimentally<sup>10</sup> that the excitation of this gyrotropic motion leads to a dynamical distortion of the vortex core profile, as predicted by micromagnetic simulations and theoretical analysis<sup>13</sup>. This distortion increases with the linear velocity of the vortex core and opposes the core polarity, until the critical velocity  $V_c \simeq 1.66\gamma\sqrt{A_{\text{ex}}}$  ( $\gamma$  is the gyromagnetic ratio of the magnetic material and  $A_{\text{ex}}$  its exchange constant) is reached and the vortex core polarity is reversed<sup>14</sup>.

In zero magnetic field, dynamical control of the polarity is difficult due to the degeneracy of the gyrotropic frequencies associated to opposite polarities  $p = \pm 1$ , which can lead to multiple core switching<sup>7,12</sup>. Still, selective core polarity reversal is possible using a circularly polarized microwave magnetic field because the sense of the core rotation is linked by a right-hand rule to its polarity<sup>8</sup>. Control of polarity switching can also be achieved by precise timing of non resonant magnetic field pulses<sup>9,19</sup>, in a similar fashion as domain wall propagation in magnetic nanowires<sup>20</sup>.

Resonant amplification<sup>21</sup> of the vortex gyrotropic motion enables to reverse the core polarity with minimum excitation power<sup>8,10,15</sup>, as it allows to concentrate the energy in a narrow frequency band. In this scheme, the damping ratio is an important parameter because it controls the minimum amplitude of the resonant excitation required to switch the core<sup>14</sup>. Here, it is shown that the damping ratio close to the reversal threshold is significantly larger than the one measured in the small oscillation regime. We associate this to the non-linear nature of the reversal process<sup>11,13</sup>.

Investigation of vortex core reversal using time-resolved imaging techniques based on X-ray magnetic circular dichroism is very powerful, as it enables direct determination of the vortex core trajectory<sup>10</sup>. However, it requires to average many events and the interpretation can become more complicated due to multiple reversal processes. In order to investigate the coupling between resonant microwave pulses and vortex dynamics near the core reversal threshold, we use a magnetic resonance force microscope (MRFM) in combination with a bias magnetic field applied perpendicularly to the disk plane, that induces two distinct resonant gyrotropic frequencies associated to opposite core polarities<sup>16,22</sup>. This frequency splitting is used for a simple, single shot reading<sup>15</sup> of the polarity state using MRFM, before and after microwave pulses have been applied to the vortex-state nano-disk.

The MRFM detection setup<sup>23</sup>, illustrated in Fig.1a, is described in the Methods section. It

allows to probe the magnetization dynamics in individual nanostructures<sup>24</sup>, and in particular to spectroscopically determine the resonance frequency of the gyrotropic mode in a vortex-state nano-disk<sup>16</sup>. The studied nano-disk with thickness 44 nm and diameter 1  $\mu\text{m}$  is made of NiMnSb alloy (see MFM image in Fig.1b), an ultra-low damping epitaxial material<sup>25</sup> (typical Gilbert constant  $\alpha_{LLG}$  is between 0.002 and 0.003). A gold antenna patterned on top allows to apply pulses of linearly polarized microwave magnetic field  $h$  in the plane of the disk.

In our experiments, we choose the bias perpendicular field  $\mu_0 H = 65$  mT in order to unambiguously discriminate the two different gyrotropic frequencies, or polarity states: resonant frequencies  $f_- = 217$  MHz and  $f_+ = 254$  MHz respectively correspond to  $p = -1$  (core antiparallel to  $H$ , see Fig.1c) and  $p = +1$  (core parallel to  $H$ , see Fig.1d). The microwave power employed to read the polarity state with MRFM is weak enough ( $P = -19$  dBm), so that  $p$  is not reversed during the reading sequence<sup>15</sup>. We also emphasize that the bias perpendicular field  $\mu_0 H = 65$  mT is almost five times smaller than the static field required to switch the core polarity<sup>16,26</sup>, so that no significant asymmetry between the two possible reversal processes ( $p = -1$  to  $p = +1$  and vice versa) is induced, as it will be clear from the data presented below.

First, we explore in Fig.2a the efficiency of single microwave pulses to switch the vortex core, depending on their duration, frequency and power.  $\Pi_-$  pulses are defined as single pulses that reverse the polarity from  $p = -1$  to  $p = +1$  and  $\Pi_+$  pulses from  $p = +1$  to  $p = -1$  (see Fig.2b). The experimental data is acquired as follows: for  $\Pi_-$  ( $\Pi_+$ ) pulses, the  $p = -1$  ( $p = +1$ ) state is first reset using an initialization pulse whose result is known to be fully deterministic<sup>15</sup>. Then, a single microwave pulse of given duration  $w$ , frequency  $f$  and power  $P$  is applied, and the final polarity state is read using MRFM. An opaque coloured pixel marks pulse settings for which reversals are recorded with a 100% success rate, while a blank pixel means that no reversal is recorded. The contour plots presented in Fig.2a with different shades of red (blue) show the superposition of the results for  $\Pi_-$  ( $\Pi_+$ ) pulses with three different durations  $w$ : 100, 50 and 20 ns.

The frequency splitting introduced by the perpendicular bias field clearly appears in Fig.2a. Due to the resonant character of the investigated switching process, a pronounced minimum in the power level required to reverse the vortex core is observed at a frequency  $f_-^*$  ( $f_+^*$ ) close to the gyrotropic frequency associated to the initial core polarity, for each duration of the  $\Pi_-$  ( $\Pi_+$ ) pulses. This frequency discrimination introduced by  $H$  allows most of the recorded results to be fully deterministic.

The minimum power  $P^*$  required to reverse the core polarity increases as the pulse duration  $w$  decreases. We have plotted the dependences on  $w$  of the optimal frequency  $f_+^*$  (Fig.2d) and of the optimal pulse energy  $E^* = P^*w$  (Fig.2e). In these plots,  $w$  ranges from 1  $\mu$ s down to 3 ns, with experimental points obtained from the analysis of data sets similar to those presented Fig.2a. There is a clear minimum in the optimal pulse energy that occurs around  $w = 50$  ns. The position of this minimum yields an estimation of the characteristic decay time. If the pulse duration exceeds this characteristic time, the vortex core dynamics reaches steady-state before the end of the pulse, i.e., the pulse duration is uselessly too long. On the contrary, if the pulse duration is shorter than this characteristic time, some energy is wasted outside the resonance line. Due to the transient response of the vortex core to the excitation pulse, the optimal frequency  $f_+^*$  measured for pulses shorter than 50 ns shifts to higher frequency<sup>14</sup> (see Fig.2d), a general behaviour of any harmonic oscillator forced on time scales shorter than its decay time.

To be more quantitative, we have performed a numerical calculation based on the analytical approach developed for zero applied magnetic field<sup>14</sup>, with the new ingredient that due to the bias perpendicular field,  $f_-$  and  $f_+$  are distinct frequencies. The trajectory of the vortex core submitted to the microwave field pulse is calculated using Thiele's equation<sup>27</sup>, and Guslienko's criterion<sup>13</sup> for core velocity is used to determine if the polarity is switched by the end of the pulse. The behaviour of the optimal pulse energy as a function of  $w$  can be reproduced with an analytical formula where the damping ratio  $d_{\text{forced}}^*$  is an adjustable parameter (blue solid line in Fig.2e). The best fit is obtained for  $d_{\text{forced}}^* = 0.018$ , corresponding to a characteristic decay time  $\tau_{\text{forced}} = 1/(d_{\text{forced}}^* 2\pi f_+) \simeq 35$  ns. The predicted optimal pulse duration is  $w_{\text{min}} = 1.26\tau_{\text{forced}} \simeq 44$  ns (see Methods section for details). Fig.2c illustrates the good agreement of the model with the experimental data of Fig.2a on the whole range of pulse parameters.

The significant result here is that the damping ratio  $d_{\text{forced}}^* = 0.018$  inferred in the forced regime close to the core reversal threshold is more than twice larger than the value measured in the small oscillation regime of the gyrotropic mode, found to be  $d_{\text{vortex}} = 0.0075$  (corresponding to a decay time  $\tau_{\text{vortex}} = 85$  ns). The damping ratio  $d_{\text{vortex}}$  is itself about three times larger than the Gilbert constant, measured from the linewidth in the perpendicularly saturated state of the NiMnSb disk and found to be  $\alpha_{LLG} = 0.0025$  (see Supplementary Figure 1). The difference between  $d_{\text{vortex}}$  and  $\alpha_{LLG}$  corresponds to the expected increase due to topological renormalization<sup>27,28</sup>. This enhancement is produced by the strongly inhomogeneous spatial distribution of magnetization in the undistorted vortex state compared to the perpendicularly saturated state. Our experimental results

of Fig.2 give a quantitative estimation of the damping ratio  $d_{\text{forced}}^*$  for the vortex distorted by large oscillations<sup>10,13</sup>. In a further step, it would be interesting to evaluate how much of the observed increase of  $d_{\text{forced}}^*$  against  $d_{\text{vortex}}$  is due to topological renormalisation between the distorted and undistorted vortex states. As can be seen in Fig.2e, a practical consequence of this increase is to decrease the optimal pulse duration  $w_{\text{min}}$  and to increase the corresponding minimum pulse energy.

Next, we investigate in Fig.3 the vortex core dynamics in the free decay regime by monitoring the core reversal induced by two consecutive microwave pulses. In these experiments, the pulse duration is set to  $w = 9$  ns and the power to  $P = -1.8$  dBm, i.e., slightly below the minimum power  $P^* = -1$  dBm required to reverse the core polarity  $p$  for such a short pulse. Contrary to a single pulse, two pulses separated by a delay  $\tau$  (Fig.3a:  $\Pi_- - \tau - \Pi_-$ ; Fig.3b:  $\Pi_+ - \tau - \Pi_+$ ) can reverse  $p$ . The striking oscillatory dependence on the pulses carrier frequency and on the delay  $\tau$  observed in Figs.3a and 3b enlightens the phase coherent coupling between the vortex gyrotropic motion and the microwave excitation. During the pulse duration, the gyrotropic motion is forced at the pulse frequency, while in the free decay regime, the core oscillates towards its equilibrium position at its natural frequency, therefore acquiring a phase shift with respect to the excitation carrier. As a result, the efficiency of the second pulse to drive the vortex core to the reversal threshold, which is estimated out of ten attempts in Fig.3, depends on the microwave frequency and on the delay between pulses in an oscillatory manner (the oscillation period scales as the inverse frequency detuning).

To illustrate further this effect of coherence, similar experiments with a  $\pi$  phase shift introduced between the two pulses have been carried out. It is clear that the regions where successful reversal are observed in Figs.3c and 3d are complementary to those in Figs.3a and 3b, respectively. Thus, phase control of the microwave excitation can trigger vortex core switching.

Using the same approach as before, it is possible to calculate numerically such experimental phase diagrams. An excellent agreement with experiments is achieved, as can be seen in Fig.4a. In Fig.4b, we have plotted the calculated vortex core trajectory and velocity as a function of time corresponding to two consecutive  $\Pi_+$  pulses at  $f = 253$  MHz separated by a 60 ns delay. In the top graphs, there is no phase shift between pulses and the time delay is such that the second pulse is efficient to amplify the gyrotropic motion from the beginning of the pulse, in contrary to the bottom graphs, where a  $\pi$  phase shift is set between pulses. As a result, the vortex core is not reversed by the end of the second pulse in the latter case, while it is in the former. The obtained data sets also allow us to fit the free decay time, and the best agreement with the experiment is

obtained for  $\tau_{\text{free}} \simeq 53$  ns. Analysis of the difference of this value with  $\tau_{\text{forced}}$  should further shed some light on the precise non-linear nature of magnetic dissipation close to the reversal threshold and on its dependence on the amplitude of the vortex core motion.

This research was partially supported by the French Grant Voice ANR-09-NANO-006-01, EU Grants DynaMax FP6-IST-033749 and Master NMP-FP7-212257. The authors acknowledge fruitful discussions with V.S. Tiberkevich, A.N. Slavin and K.Y. Guslienko.

## METHODS

### A. Sample preparation.

The magnetic nano-disk (thickness 44 nm, diameter 1  $\mu\text{m}$ ) was patterned by standard e-beam lithography and ion-milling techniques from an extended film of NiMnSb grown by molecular-beam epitaxy on an InP(001) substrate<sup>29</sup>. A 50 nm thick  $\text{Si}_3\text{N}_4$  cap layer was deposited on top of the disk for protection and a broadband coplanar microwave antenna (300 nm thick Au) was subsequently evaporated on top of the patterned disk. The width of the antenna constriction above the disk is 5  $\mu\text{m}$  (see Supplementary Figure 2).

### B. Microwave setup.

Injecting a microwave current from a synthesizer inside the antenna produces an in-plane linearly polarized microwave magnetic field  $h$ , oriented perpendicular to the stripe direction. In order to apply two consecutive pulses separated by a variable delay  $\tau$ , the carrier of the cw excitation is split into two branches, each of them being gated by independent mixers before being recombined. A phase shift can be introduced between the two branches using a delay line. The typical rise and fall times of pulses are 0.8 ns and the control on the delay  $\tau$  is better than 0.1 ns. The calibration of the amplitude of  $h$  yields the value  $\mu_0 h = 1.05$  mT with an error bar of 25% for a 0 dBm input power in the antenna. Therefore, the microwave power range in Fig.2a corresponds to microwave field amplitude ranging from 0.2 to 0.7 mT, the power in double pulses experiments of Fig.3a to  $\mu_0 h = 0.85$  mT, and the power employed to read the polarity to  $\mu_0 h = 0.1$  mT.

### C. Initialization pulse.

A  $\Pi_+$  pulse with settings ( $w = 50$  ns,  $f = f_+$ ,  $P = -11$  dBm)<sup>15</sup> is used to set the initial polarity state to  $p = -1$ . In fact, such an initialization pulse does not affect the  $p = -1$  state and it transforms  $p = +1$  into  $p = -1$  (see Fig.2a). Similarly, a  $\Pi_-$  pulse ( $w = 50$  ns,  $f = f_-$ ,  $P = -11$  dBm) is used to set the initial polarity state to  $p = +1$ .

### D. MRFM detection.

The MRFM setup<sup>23</sup> is located inside a vacuum chamber ( $10^{-6}$  mbar) and operates at room temperature. The cantilever is an Olympus Biolever (spring constant  $k \simeq 5$  mN/m) with a 800 nm diameter sphere of soft amorphous Fe (with 3% Si) glued to its apex. MRFM spectroscopy is achieved by placing the centre of the magnetic spherical probe above the centre of the NiMnSb nano-disk. The separation between the sample and the probe is  $s = 1.5$   $\mu$ m. The probe senses the dipolar force  $F_z$  proportional to the perpendicular component  $M_z$  of the magnetization of the nano-disk (see Fig.1a). Ferromagnetic resonance spectra are obtained as a function of the microwave excitation frequency at a fixed bias field  $H$ . The microwave modulation is a cyclic absorption sequence, where the microwave power is switched on and off at the cantilever resonance frequency,  $f_c \simeq 11.8$  kHz. The MRFM signal originates from the cyclic diminution of  $M_z$  of the nano-disk synchronous with the absorption of the microwave field<sup>16,23</sup>. The resulting force modulated at the mechanical resonance of the cantilever force produces a cantilever vibration amplitude enhanced by its quality factor  $Q \simeq 4000$ , that is optically detected.

### E. Numerical calculations.

The calculations presented in Figs.2 and 4 are based on linearised Thiele's equation<sup>27</sup>, an effective equation of motion for the vortex core position  $\mathbf{X}$  in the disk plane:

$$-\mathbf{G} \times \dot{\mathbf{X}} - \hat{D} \dot{\mathbf{X}} + \kappa \mathbf{X} + \mu[\hat{\mathbf{z}} \times \mathbf{h}] = 0. \quad (1)$$

The first term is the gyroforce ( $\mathbf{G}$  is the gyrovector), the second one is the damping ( $d = -D/|G|$ ), the third one is the restoring force ( $\kappa$  is the stiffness coefficient), and the last one is the Zeeman energy with the spatially uniform external field  $\mathbf{h}$  ( $\hat{\mathbf{z}}$  is the unit vector normal to the disk plane and details on  $\mu$  and previously mentioned coefficients can be found in refs.<sup>3,28</sup>). The resonant

frequency of vortex core gyration is  $\omega_G = \kappa/|G|$ . From Eq.1 one can find the instantaneous position  $\mathbf{X}(t)$  and the velocity  $v(t)$  of the vortex core in the presence or absence of the harmonic excitation field  $h(t)$ , as derived in the supplementary documents of ref.<sup>14</sup>. If Gusliencko's criterion on critical velocity<sup>13</sup> is met at some time of the simulated pulse sequence ( $v(t) > V_c$ ), the vortex core is assumed to have switched. Experimental sample size, gyrotropic frequencies  $f_-$  and  $f_+$  associated to each polarity, and non-linear redshift of the frequency (3%) are used in our calculation. The minimal excitation amplitude  $h_c(\omega, w)$  to reach  $V_c$  by the end of the pulse depends<sup>14</sup> on the excitation frequency  $\omega$  and on the pulse duration  $w$ . Minimization of the energy  $E \propto wh_c^2(\omega, w)$  with respect to  $\omega$  yields the dependence on  $w$  of the optimal frequency  $f_+^*$  plotted in Fig.2d and of the optimal pulse energy  $E^*$  plotted in Fig.2e:

$$E^*(w) = w \frac{h_c^2(w)}{a} = \left( \frac{6dV_c}{a\gamma R} \right)^2 \frac{w}{1 + e^{-2d\omega_G w} - 2e^{-d\omega_G w}}. \quad (2)$$

In this expression,  $a$  is an experimental conversion factor between the input power in the antenna and  $h^2$  determined from calibration. Therefore, two independent parameters are used to adjust the calculation with the data in Fig.2e: the damping ratio  $d$  to fit the overall shape (position of minimum) and the critical velocity  $V_c$  to fit the absolute value of the energy. The optimal pulse duration  $w_{\min}$  corresponding to the minimum energy  $E_{\min}^*$  follows from Eq.2:  $w_{\min} = 1.26/(d_{\text{forced}}^* \omega_G) = 1.26\tau_{\text{forced}}$  (for the blue solid line in Fig.2e,  $d_{\text{forced}}^* = 0.018$ ,  $\tau_{\text{forced}} = 35$  ns, hence  $E_{\min}^*$  is reached for  $w_{\min} = 44$  ns). The fitted critical velocity in our NiMnSb disk is  $V_c \simeq 190$  m/s, in good agreement with the expected value<sup>14</sup> of 225 m/s (the exchange constant of NiMnSb is  $A_{\text{ex}} = 6$  pJ/m<sup>30</sup>). The same parameters are used in calculations of Figs.2 and 4. In Fig.4, the only new fitting parameter is the characteristic time  $\tau_{\text{free}}$  of the vortex core free decay (the relaxation is assumed to be exponential). We also allow a fine adjustment of the phase shift between the two pulses in order to get the best agreement with the data (25° in the “zero phase shift” experiment and 190° in the “ $\pi$  phase shift” experiment; these small differences are ascribed to an imperfect delay line in the experimental pulse setup).



---

\* Corresponding author: gregoire.deloubens@cea.fr

† Present address: Institut für Physik, Martin-Luther-Universität, Halle Wittenberg, 06099 Halle, Germany

- <sup>1</sup> Miramond, C., Fermon, C., Rousseaux, F., Decanini, D. & Carcenac, F. Permalloy cylindrical submicron size dot arrays. *J. Magn. Magn. Mater.* **165**, 500–503 (1997).
- <sup>2</sup> Cowburn, R. P., Koltsov, D. K., Adeyeye, A. O., Welland, M. E. & Tricker, D. M. Single-domain circular nanomagnets. *Phys. Rev. Lett.* **83**, 1042–1045 (1999).
- <sup>3</sup> Guslienko, K. Y. Magnetic vortex state stability, reversal and dynamics in restricted geometries. *J. Nanosci. Nanotechnol.* **8**, 2745–2760 (2008).
- <sup>4</sup> Shinjo, T., Okuno, T., Hassdorf, R., Shigeto, K. & Ono, T. Magnetic vortex core observation in circular dots of permalloy. *Science* **289**, 930–932 (2000).
- <sup>5</sup> Wachowiak, A. *et al.* Direct observation of internal spin structure of magnetic vortex cores. *Science* **298**, 577–580 (2002).
- <sup>6</sup> Waeyenberge, B. V. *et al.* Magnetic vortex core reversal by excitation with short bursts of an alternating field. *Nature* **444**, 461–464 (2006).
- <sup>7</sup> Yamada, K. *et al.* Electrical switching of the vortex core in a magnetic disk. *Nature Mater.* **6**, 270–273 (2007).
- <sup>8</sup> Curcic, M. *et al.* Polarization selective magnetic vortex dynamics and core reversal in rotating magnetic fields. *Phys. Rev. Lett.* **101**, 197204 (2008).
- <sup>9</sup> Weigand, M. *et al.* Vortex core switching by coherent excitation with single in-plane magnetic field pulses. *Phys. Rev. Lett.* **102**, 077201 (2009).
- <sup>10</sup> Vansteenkiste, A. *et al.* X-ray imaging of the dynamic magnetic vortex core deformation. *Nature Physics* **5**, 332–334 (2009).
- <sup>11</sup> Hertel, R. & Schneider, C. M. Exchange explosions: Magnetization dynamics during vortex-antivortex annihilation. *Phys. Rev. Lett.* **97**, 177202 (2006).
- <sup>12</sup> Hertel, R., Gliga, S., Fähnle, M. & Schneider, C. M. Ultrafast nanomagnetic toggle switching of vortex cores. *Phys. Rev. Lett.* **98**, 117201 (2007).
- <sup>13</sup> Guslienko, K. Y., Lee, K.-S. & Kim, S.-K. Dynamic origin of vortex core switching in soft magnetic nanodots. *Phys. Rev. Lett.* **100**, 027203 (2008).

- <sup>14</sup> Lee, K.-S. *et al.* Universal criterion and phase diagram for switching a magnetic vortex core in soft magnetic nanodots. *Phys. Rev. Lett.* **101**, 267206 (2008).
- <sup>15</sup> Pigeau, B. *et al.* A frequency-controlled magnetic vortex memory. *Appl. Phys. Lett.* **96**, 132506 (2010).
- <sup>16</sup> de Loubens, G. *et al.* Bistability of vortex core dynamics in a single perpendicularly magnetized nanodisk. *Phys. Rev. Lett.* **102**, 177602 (2009).
- <sup>17</sup> Park, J. P., Eames, P., Engebretson, D. M., Berezovsky, J. & Crowell, P. Imaging of spin dynamics in closure domain and vortex structure. *Phys. Rev. B* **67**, 020403(R) (2003).
- <sup>18</sup> Novosad, V. *et al.* Magnetic vortex resonance in patterned ferromagnetic dots. *Phys. Rev. B* **72**, 024455 (2005).
- <sup>19</sup> Keavney, D. J., Cheng, X. M. & Buchanan, K. S. Polarity reversal of a magnetic vortex core by a unipolar, nonresonant in-plane pulsed magnetic field. *Appl. Phys. Lett.* **94**, 172506 (2009).
- <sup>20</sup> Thomas, L. *et al.* Oscillatory dependence of current-driven magnetic domain wall motion on current pulse length. *Nature* **443**, 197–200 (2006).
- <sup>21</sup> Thirion, C., Wernsdorfer, W. & Mailly, D. Switching of magnetization by nonlinear resonance studied in single nanoparticles. *Nature Mater.* **2**, 524–527 (2003).
- <sup>22</sup> Ivanov, B. A. & Wysin, G. M. Magnon modes for a circular two-dimensional easy-plane ferromagnet in the cone state. *Phys. Rev. B* **65**, 134434 (2002).
- <sup>23</sup> Klein, O. *et al.* Ferromagnetic resonance force spectroscopy of individual submicron-size samples. *Phys. Rev. B* **78**, 144410 (2008).
- <sup>24</sup> de Loubens, G. *et al.* Magnetic Resonance Studies of the Fundamental Spin-Wave Modes in Individual Submicron Cu/NiFe/Cu Perpendicularly Magnetized Disks. *Phys. Rev. Lett.* **98**, 127601 (2007).
- <sup>25</sup> Heinrich, B. *et al.* Magnetic properties of NiMnSb(001) films grown on InGaAs/InP(001). *J. Appl. Phys.* **95**, 7462 (2004).
- <sup>26</sup> Thiaville, A., García, J. M., Dittrich, R., Miltat, J. & Schrefl, T. Micromagnetic study of bloch-point-mediated vortex core reversal. *Phys. Rev. B* **67**, 094410 (2003).
- <sup>27</sup> Thiele, A. A. Steady-state motion of magnetic domains. *Phys. Rev. Lett.* **30**, 230–233 (1973).
- <sup>28</sup> Guslienko, K. Y. Low-frequency vortex dynamic susceptibility and relaxation in mesoscopic ferromagnetic dots. *Appl. Phys. Lett.* **89**, 022510 (2006).
- <sup>29</sup> Bach, P. *et al.* Molecular-beam epitaxy of the half-heusler alloy NiMnSb on (In,Ga)As/InP(001). *Appl. Phys. Lett.* **83**, 521 (2003).

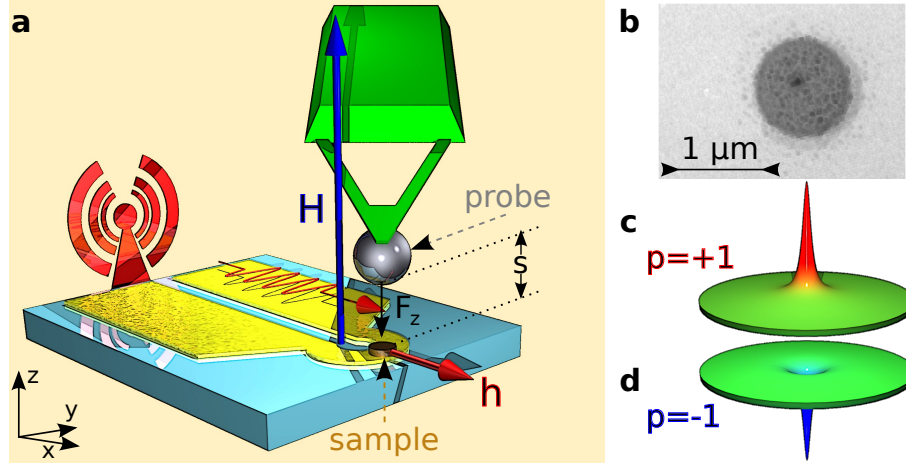
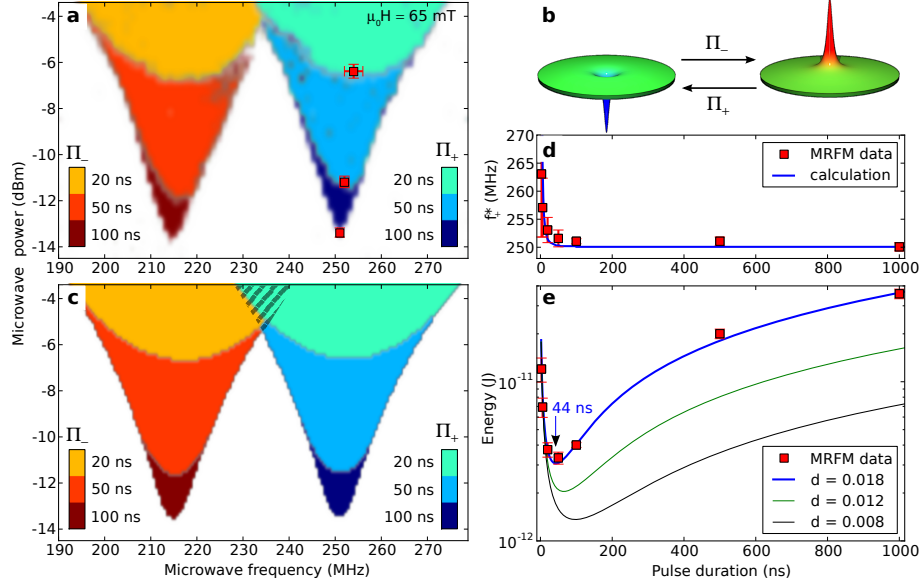


FIG. 1. **Experimental setup and sample.** **a**, A magnetic resonance force microscope (see Methods) is used to probe the vortex core dynamics of an individual vortex-state NiMnSb disk (diameter  $1\ \mu\text{m}$ , thickness  $44\ \text{nm}$ ). A soft cantilever, with a spherical magnetic probe attached at its end and placed at a distance  $s = 1.5\ \mu\text{m}$  from the sample, detects mechanically the vortex core dynamics. The bias magnetic field  $H$  is applied perpendicularly to the disk plane whereas microwave pulses of linearly polarized field  $h$  are applied in the plane. **b**, Zero-field magnetic force image of the magnetic vortex, where the dark spot at the disk centre reveals the core prepared in the  $p = +1$  (**c**) polarity state. The opposite configuration is the  $p = -1$  (**d**) polarity state.

<sup>30</sup> Ritchie, L. *et al.* Magnetic, structural, and transport properties of the heusler alloys Co<sub>2</sub>MnSi and NiMnSb. *Phys. Rev. B* **68**, 104430 (2003).



**FIG. 2. Vortex core resonant reversal by a single microwave pulse.** **a**, Efficiency of the  $\Pi_-$  and  $\Pi_+$  pulses (see panel **b**) to reverse the vortex core at  $\mu_0 H = 65$  mT measured as a function of power and frequency (stepped by increments of 0.3 dBm and 1.2 MHz). For each pulse type, a coloured pixel ( $\Pi_-$ : red shade,  $\Pi_+$ : blue shade) marks a successful reversal. The transparency gives the switching probability averaged over 16 attempts. Experiments corresponding to three values of the pulse duration  $w$  are displayed. For each  $w$  we define  $(f_+^*, P^*)$ , the optimal working point of the  $\Pi_+$  pulse located at the bottom of the corresponding contour plot (see **a**). **c**, Numerical calculation (see Methods) of the experiments presented in **a**. This calculation is not valid within the shaded area, where multiple vortex core reversals can occur. **d, e**, Experimental (**■**) and calculated (lines) dependences on  $w$  of the optimal frequency  $f_+^*$  (**d**) and of the optimal pulse energy  $E^* = P^* w$  (**e**). The experimental points are obtained from the analysis of data sets similar to those presented in **a**, where  $w$  is varied from 1  $\mu$ s down to 3 ns (the three **■** close to the minimum energy in **e** are inferred from those displayed in **a**). The best agreement is obtained for a damping ratio  $d_{\text{forced}}^* = 0.018$ , i.e., a characteristic decay time  $\tau_{\text{forced}} = 35 \pm 4$  ns. The absolute value of the energy is also fitted in the calculation, which enables to extract the critical velocity for vortex core reversal,  $V_c \simeq 190$  m/s (see Methods). Error bars on  $f_+^*$  and  $E^*$  are absolute minima and maxima resulting from experimental uncertainties in **a** on the optimal working point  $(f_+^*, P^*)$  associated to each pulse duration.

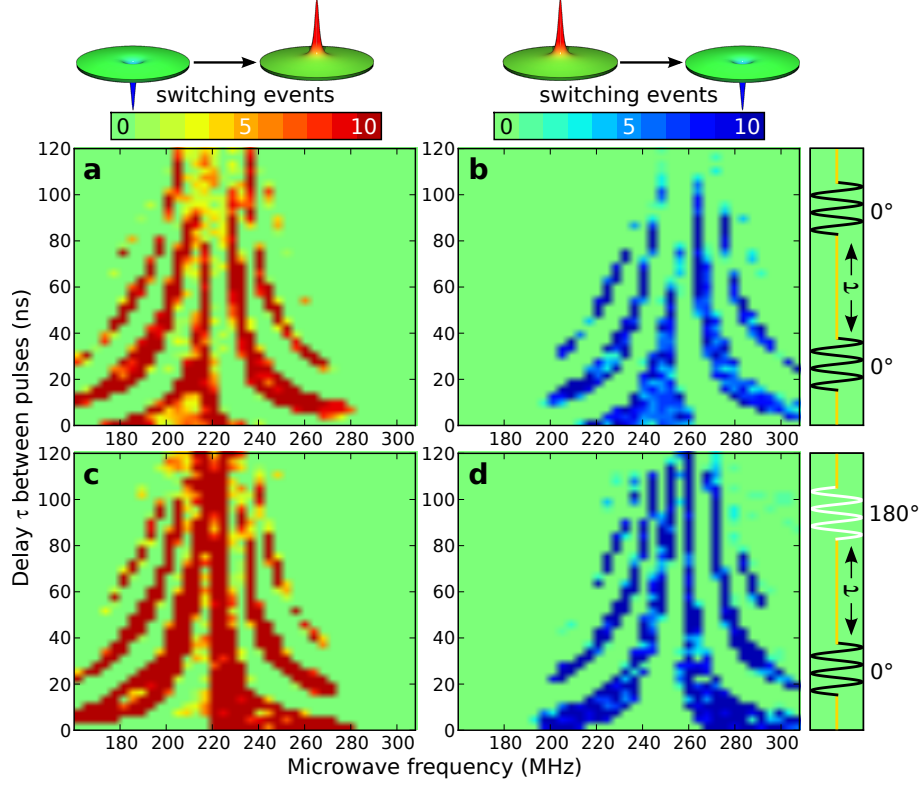
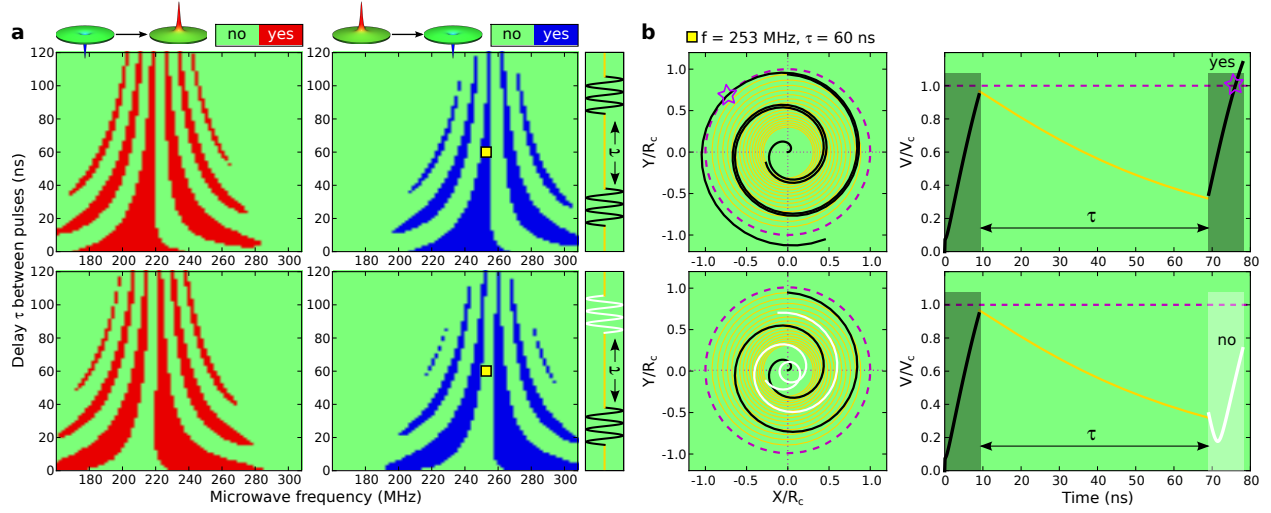


FIG. 3. **Oscillatory dependence on frequency and delay between two consecutive pulses of the vortex core reversal efficiency.** **a–d**, Number of switching events out of ten attempts as a function of the delay  $\tau$  separating the two pulses ( $w = 9$  ns,  $P = -1.8$  dBm) and of the carrier microwave frequency (stepped by increments of 3 ns and 4 MHz, respectively). The bias magnetic field is  $\mu_0 H = 65$  mT. The initial polarity state is  $p = -1$  in the left graphs (**a**, **c**) and  $p = +1$  in the right graphs (**b**, **d**). As depicted in the right-side panels, the phase difference between the two pulses is zero in the upper graphs (**a**, **b**) and  $\pi$  in the lower graphs (**c**, **d**).



**FIG. 4. Phase coherent control of vortex core reversal.** **a**, Numerical calculation (see Methods) of the double pulse sequences presented in Fig.3. The best agreement is obtained for a characteristic decay time  $\tau_{\text{free}} = 53 \pm 6$  ns in the free regime. **b**, Associated vortex core trajectory (left) and velocity (right) vs. time plotted for two  $\Pi_+$  pulses with settings  $\tau = 60$  ns and  $f = 253$  MHz (see pixel  $\blacksquare$  in **a**). For these settings, the vortex core is reversed when the phase difference between the pulses is equal to zero (top, see star) and not reversed when it is equal to  $\pi$  (bottom).

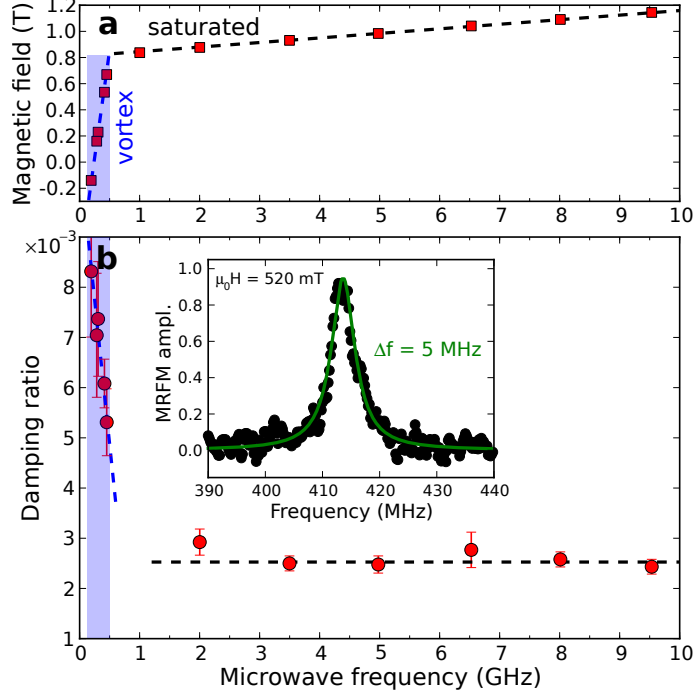


FIG. 5. (Supplementary Figure 1) **Damping ratio in the small oscillation regime.** **a**, Frequency–perpendicular field dispersion relation of the uniform mode in the saturated state ( $\mu_0 H > 0.8$  T) and of the gyrotropic mode in the vortex state ( $\mu_0 H < 0.8$  T). Dashed lines are analytical expressions (Eqs. 1 and 2 in ref.<sup>16</sup>). **b**, Dependence on frequency of the damping ratio obtained from MRFM spectroscopic measurements in the small oscillation regime (the typical power level is  $-30$  dBm, corresponding to  $\mu_0 h = 0.03$  mT). Dashed lines are guides to the eye. Lorentzian fits of the resonance peaks (inset shows such a fit at a fixed field in the vortex state) yield the centre frequency  $f$  and the frequency linewidth  $\Delta f$  together with the associated error bars, hence the damping ratio  $d = \Delta f / (2f)$ . The damping ratio in the saturated state is equal to the Gilbert constant  $d = \alpha_{LLG} = 0.0025$ . In the vortex state, the damping ratio is renormalized by topology (Eq.13b in ref.<sup>27</sup>). Experimentally, it increases from about 0.005 to 0.008 as the frequency decreases from 450 MHz down to 190 MHz (i.e., the perpendicular field decreases from 0.65 T down to  $-0.15$  T). Close to  $H = 0$ , the experimental value  $d = d_{\text{vortex}} = 0.0075 \pm 0.001$  corresponds to a decay time  $\tau_{\text{vortex}} = 1/(\pi \Delta f) = 85 \pm 12$  ns and is in good agreement with the predicted value<sup>28</sup>  $d_{\text{vortex}} = \alpha_{LLG} [1 + \ln(R/b)/2] \simeq 0.007$  ( $R = 500$  nm and  $b \simeq 15$  nm are respectively the disk and vortex core radii).

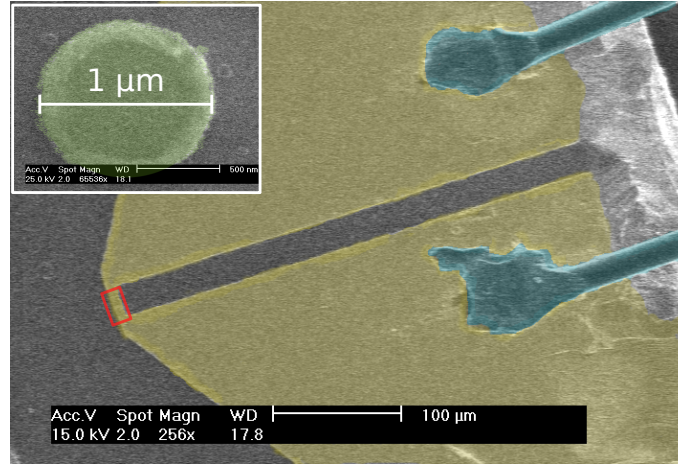


FIG. 6. (Supplementary Figure 2) **Microwave antenna and NiMnSb disk sample.** Scanning electron microscopy (SEM) image of the microwave antenna where the red rectangle points out the  $5\ \mu\text{m}$  wide constriction under which the NiMnSb disk (diameter  $1\ \mu\text{m}$ , thickness  $44\ \text{nm}$ ) is located (see insert). The microwave antenna is wire bounded to a coplanar waveguide on the right side.